ACS NANO

www.acsnano.org

ARTICLE

Anisotropic Signal Processing with Trigonal Selenium Nanosheet Synaptic Transistors

Jing-Kai Qin, Feichi Zhou, Jingli Wang, Jiewei Chen, Cong Wang, Xuyun Guo, Shouxin Zhao, Yi Pei, Liang Zhen, Peide D. Ye, Shu Ping Lau, Ye Zhu, Cheng-Yan Xu, and Yang Chai*

Cite This: *ACS Nano* 2020, 14, 10018−10026

Read Online

ACCESS | Metrics & More | Article Recommendations | Supporting Information

ABSTRACT: **Hardware implementation of an artificial neural network requires neuromorphic devices to process information with low energy consumption and high heterogeneity. Here we demonstrate an electrolyte-gated synaptic transistor (EGT) based on a trigonal selenium (*t*-Se) nanosheet. Due to the intrinsic low conductivity of the Se channel, the *t*-Se synaptic transistor exhibits ultralow energy consumption, less than 0.1 pJ per spike. More importantly, the intrinsic low symmetry of *t*-Se offers a strong anisotropy along its *c*- and *a*-axis in electrical conductance with a ratio of up to 8.6. The multiterminal EGT device exhibits an anisotropic response of filtering behavior to the same external stimulus, which enables it to mimic the heterogeneous signal transmission process of the axon−multisynapse biostructure in the human brain. The proof-of-concept device in this work represents an important step to develop neuromorphic electronics for processing complex signals.**

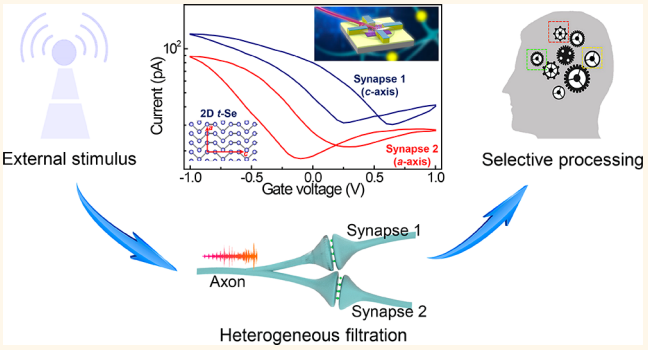

KEYWORDS: *electrolyte-gated transistor, synaptic device, t-Se nanosheet, van der Waals crystals, anisotropic response*

Bioinspired processing units require a device with variable "interconnection" strength or plasticity.[1−5] The three-terminal electrolyte-gated transistor (EGT) is regarded as a promising candidate for realizing neuromorphic functions and mimicking the behaviors of the human brain with low power consumption and a variety of functionalities.[6−11] Unlike the two-terminal resistive switching memristors,[12−14] the three-terminal EGT device can decouple the "read" and "write/erase" process, in which the voltage pulse applied on the gate terminal acts as a "write/erase" operation, and the "read" operation is performed along the source−drain terminals. The ions (H^+, Li^+, Na^+, *etc.*) in the electrolyte gate can migrate or accumulate at the electrolyte/semiconductor interface to form double-layer capacitance or inject into channel materials under the programming voltage stimulus, resulting in the change of channel conductance. This characteristic of EGT devices plays an important role in achieving high-performance artificial neural systems with high reversibility, low-power dissipation, multiple states, and near-linear modulation of channel conductance.

The synaptic devices are required to be capable of operating with extremely low energy consumption (only 1−100 fJ per synaptic event in biological neural networks).[15] Therefore, channel materials with inherently low conductivity are highly desirable for minimizing power consumption. In addition, the realization of heterogeneity in plasticity is also critical for the building of an artificial neural network with high complexity.[16−19] For example, in the typical axon−multisynapse biostructure of the human brain, the neural signals from the preaxon can be filtered and transmit heterogeneously to the postsynapses by controlling the synaptic weight,[20] leading to the selective response of the neuron to the same external stimulus. The EGT devices can be used to mimic the functional roles of the axon−multisynapse system, in which the gate electrode acts as a presynapse, transmitting signals from the axon, and the multiterminal devices with the same channel represent the postsynapses. It requires the channel material to dissimilarly respond to external voltage stimulation.

In this work, we adopt a van der Waals trigonal-selenium (vdW *t*-Se) nanosheet as a channel material of EGT devices, which present a low energy consumption of 0.1 pJ. The transition from short-term plasticity (STP) to long-term

Received: April 14, 2020
Accepted: August 4, 2020
Published: August 4, 2020

https://dx.doi.org/10.1021/acsnano.0c03124
ACS Nano 2020, 14, 10018−10026

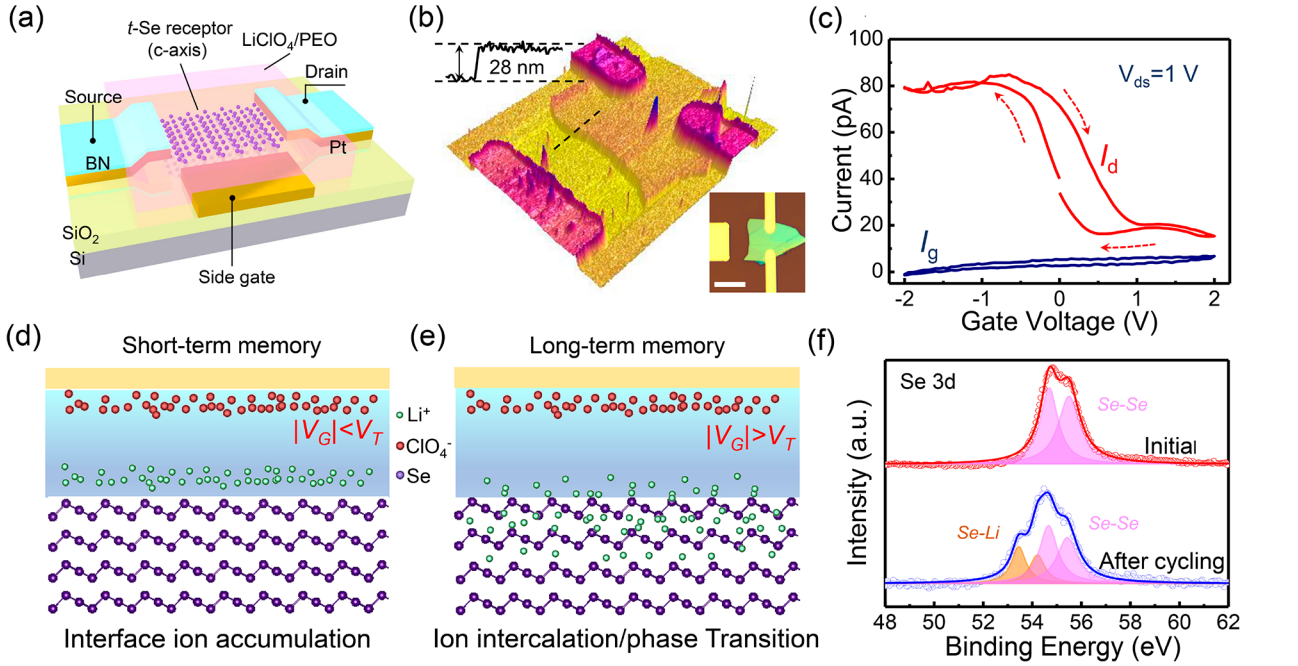

Figure 1. (a) Schematic illustration showing the three-terminal electrolyte-gated transistor to mimic the biological behavior of the synapse. The voltage pulse applied on the side gate could act as a "write" operation, while the "read" operation is complemented on the source−drain of the devices. (b) AFM image of the device before electrolyte dropping. The line profile shows the thickness of *t*-Se is 28 nm. Inset image is the optical microscopy of the same device, and the scale bar is 10 μm. (c) Typical transfer curve of the EGT device at V_{ds} = 1 V swept at 20 mV s^{-1}. (d, e) The modulation mechanism of channel conductance in EGT devices with different applied voltage. As the $V_G < V_T$, only an EDL is constructed at the electrolyte/*t*-Se interface, while the high V_G would drive Li ions into the *t*-Se lattice and result in a phase change. (f) High-resolution XPS Se 3p spectra of the *t*-Se nanosheet before and after Li^+ intercalation.

plasticity (LTP) can also be selectively realized by tuning the amplitude of the gate voltage. More importantly, a large anisotropic factor of electrical resistance (~8.6) in *t*-Se was demonstrated, which is among the highest in other reported 2D anisotropic materials. Due to the intrinsic anisotropy in electronic properties, we demonstrate a dissimilarly synaptic response of multiterminal EGT devices, exhibiting its great potential for developing an artificial system to mimic the behaviors of the human brain.

RESULTS AND DISCUSSION

Figure 1a presents the schematic structure of three-terminal *t*-Se EGT devices. The *t*-Se nanosheet was used as a channel material with a length of 10 μm. A $LiClO_4$/PEO (mass ratio of 1:9) electrolyte was directly dropped, covering both the electrodes and the device channel. An insulating hexagonal boron nitride (*h*-BN) nanosheet was transferred on the top surface of the source−drain electrodes to minimize the leakage current from the gate electrode. Upon applying presynaptic voltage from the side gate, Li^+ and ClO_4^- ions can easily move forward/backward in the electrolyte, resulting in the modulation of the channel conductance. We choose highly anisotropic and less conductive *t*-Se nanosheets as channel materials, which are prepared using a physical vapor deposition (PVD) technique. Figure 1b shows the typical atomic force microscopy and optical image of the device. The atomic structure of *t*-Se nanosheets consists of parallel one-dimensional (1D) atomic chains. The nanosheets exhibit an irregular quadrangular shape with the straight edge along the *c*-axis direction, which can be confirmed by the high-resolution transmission electron microscopy (HRTEM) characterization (Supporting Information Figure S1a,b). In addition, combined with the results of Raman spectra (see details in Supporting Information Figure S1c,d and related discussion), we can also unambiguously determine the crystallizing orientation of *t*-Se nanosheets.[21]

Figure 1c presents the typical transfer characteristics of the EGT devices. Due to the intimate encapsulation of source−drain electrodes by the *h*-BN nanosheet, the gate current (I_g) is negligible compared with the drain current (I_{ds}). As the gate voltage (V_g) sweeps from 0 to −2 V, I_{ds} increases from 40 pA to 85 pA with a quick saturation at V_g = −0.9 V, and it drops slowly as the voltage is swept back to 2 V, showing a typical p-type transport behavior. The testing environment has a negligible influence on the performance of devices because the solid-state electrolyte isolates the channel from the ambient environment. As shown in typical transfer curves (Supporting Information Figure S2), the curve of the as-fabricated device in air condition is close to that achieved in a vacuum environment. After a 3-day exposure in air, insignificant degradation of the electrical properties was observed, exhibiting an excellent air stability. By applying a positive gate voltage, Li^+ ions in the electrolyte can relax from the PEO chains and move toward the *t*-Se side, while ClO_4^- will flow along the opposite direction. The accumulation of Li^+ ions at the electrolyte/channel interface will first result in the formation of electrical double layer (EDL) capacitance and modulation of the channel conductance (Figure 1d). However, the accumulated ions at the interface will relax after removing the gate voltage, and the temporary change of carrier density in the channel will decay gradually.[22,23] By increasing the amplitude of the positive gate voltage, Li^+ ions can intercalate into the lattice of the top *t*-Se layers (Figure 1e). It can trigger the reversible intercalation between Li^+ ions and *t*-Se, resulting

https://dx.doi.org/10.1021/acsnano.0c03124
ACS Nano 2020, 14, 10018−10026

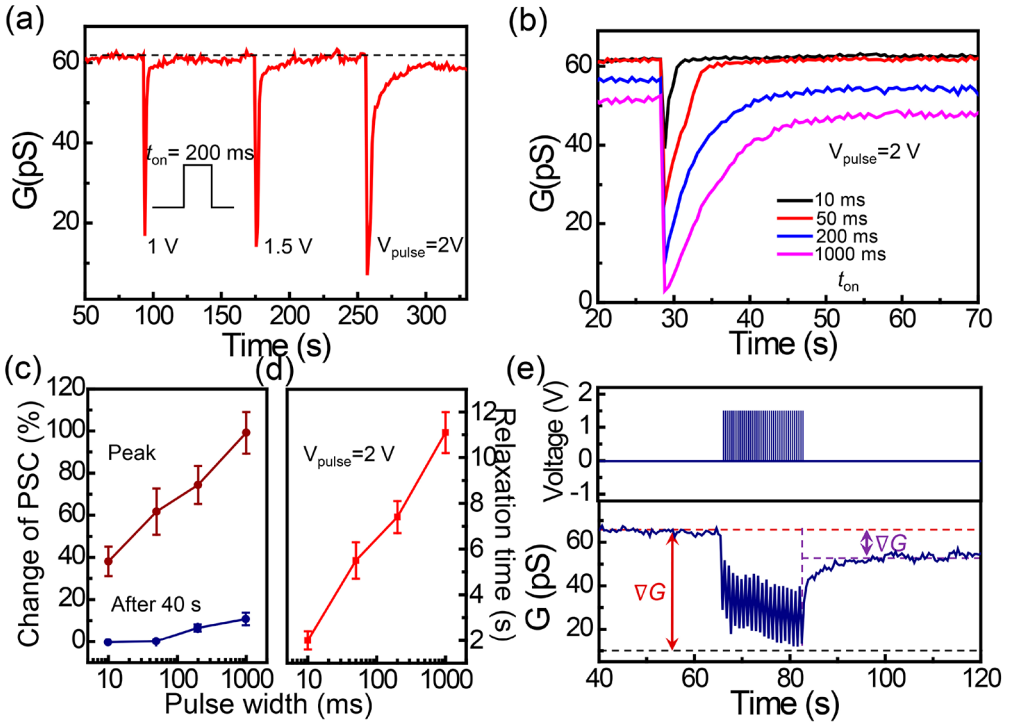

Figure 2. (a) Channel conductance of the device stimulated by different gate voltage pulses (1.0, 1.5, and 2.0 V) with the same width time (200 ms). (b) Channel conductance of a device spiked by a positive gate voltage pulse (2 V) with different width times (10, 50, 200, and 1000 ms). (c, d) The change ratio of the postsynaptic current and relaxation time as a function of gate voltage pulse width for a single pulse (2 V) event. (e) Depression process of the synapse mimicked by successive gate voltage spikes with intervals of 1 s (V_g = 1.5 V, t_{on} = 200 ms).

in the formation of a Li_xSe phase with lower conductivity and the reduction of channel electrical conductance.[24−26] This result matches well our theoretical calculations (Supporting Information Figure S3), where the new phase induced by Li^+ intercalation is expected to have a larger band gap compared with intrinsic *t*-Se. An X-ray photoelectron spectroscopy (XPS) spectrum was conducted on the *t*-Se nanosheet after removing the solid-state electrolyte by methanol, and the shift of the Se 3d peak toward lower binding energy strongly suggests the presence of Li_xSe (Figure 1f).[27] A clear red shift of Raman peaks of the *t*-Se channel was also observed after cycling (Supporting Information Figure S4), which is attributed to the phase change as well as the charge transfer between Li^+ ions and *t*-Se.[28] The integrity of the *t*-Se nanosheet was well maintained after removing the electrolyte (Supporting Information Figure S5). The thickness increases slightly from the original 22 nm to 28 nm, and it is consistent with the cross-section TEM characterization, where a distinct thickness increase of *t*-Se can be observed after the Li^+ intercalation. The transfer curve of the device shows a significant drop of on-state current. The change of thickness and electrical performance can be understood as a result of the phase change from Se to Li_xSe occurring during Li^+ intercalation. In this way, the change of channel conductance can be well maintained after the voltage was removed. The short-term and long-term modulation of the channel conductance in EGT devices can be used to emulate the STP and LTP of synapses in biological systems, respectively.

In the EGT device, the voltage pulses (V_{pulse}) applied on the electrolyte are analogous to the presynaptic spikes in a biological neuron, which induces an excitatory/inhibitory postsynaptic current (EPSC/IPSC) in the postsynapse. We adopt channel conductance (G) to evaluate the EPSC in the EGT devices. As shown in Figure 2a, spike amplitude dependent G is measured with a fixed source−drain voltage of 1 V. The amplitude of the pulse is set to be 1.0, 1.5, and 2.0 V with the same time width (t_{on}) of 200 ms. G increases sharply to the peak and then slowly decays back to the original value at V_{pulse} = 1 V, indicating a short-term change of postsynaptic current (PSC). Such volatile memorizing characteristics can be attributed to the relaxation of Li^+ ions accumulated at the electrode/channel interface. The peak value of G increases with the amplitude of the gate voltage, and it cannot be restored back to the resting current at V_{pulse} = 2 V even after 40 s of stimulus, which means a long-term modulation of channel conductance occurs under a high-voltage stimulus. We can define the change ratio of ΔG as $((G_1 - G_0)/G_0) \times 100\%$, where G_0 represents the initial channel conductance, while G_1 is a value obtained after the stimulation of the voltage pulse. The long-term ΔG of the *t*-Se EGT device was calculated to be −6% with a V_{pulse} of 2 V. The dependence of channel conductance on the pulse width (t_{on}) at fixed amplitude (2 V) was investigated (Figure 2b and c). The corresponding relaxation time t_{relax}, which is defined as the time taken for the conductance to increase to 10%, was extracted and plotted (Figure 2d). The change of G and t_{relax} increase as a function of t_{on}, and the highest long-term ΔG of −11% and t_{relax} of 10.5 s are achieved at t_{on} = 1000 ms. These results can be well reproduced in more devices with different thicknesses. The hysteresis in the transfer curve caused by the Li^+ intercalation/extraction can be clearly observed and well reproduced (Supporting Information Figure S6), and all the devices exhibit a clear long-term change of channel conductance after applying a single gate pulse (2 V, 1000 ms). We also summarized the long-term change of PSC ($\Delta G/G_0$) of the devices (Supporting Information Figure S7), and it

https://dx.doi.org/10.1021/acsnano.0c03124
ACS Nano 2020, 14, 10018−10026

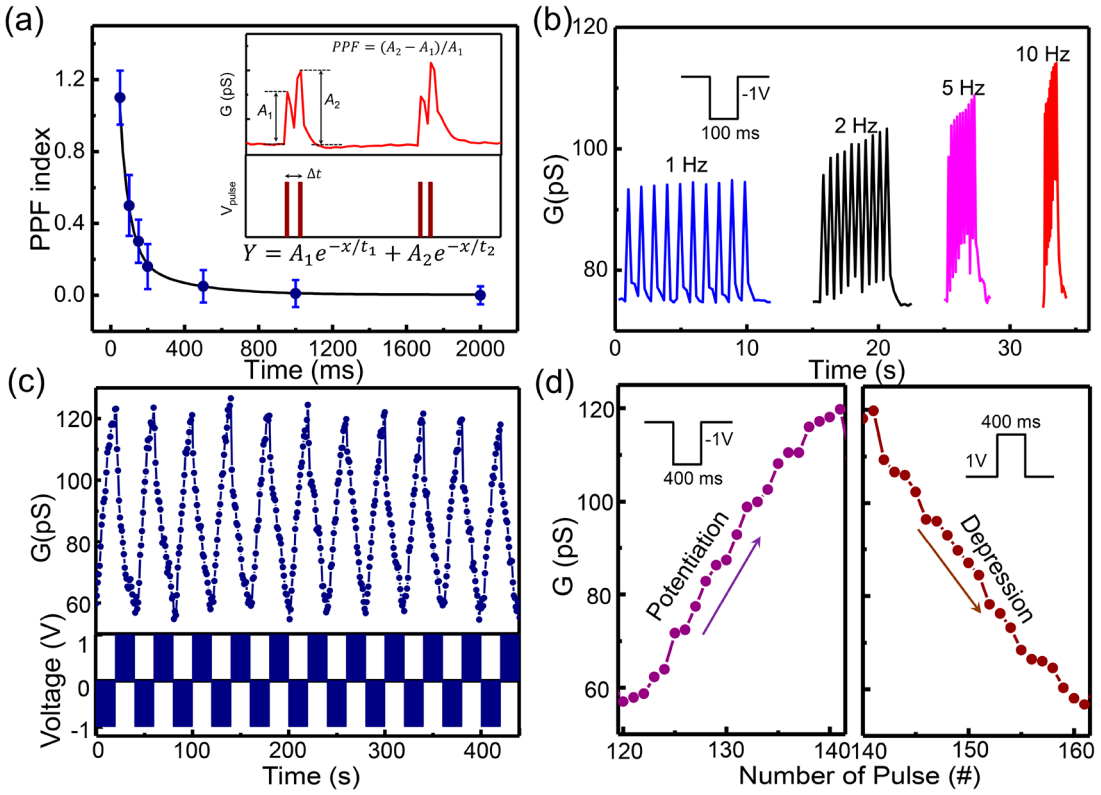

Figure 3. (a) PPF index as a function of time duration, defined as $(A_2 - A_1)/A_1$, where A_1 and A_2 are the amplitudes of the first and second channel conductance (G), plotted as a function of pulse interval (Δt). Inset: Channel conductance stimulated by a pair of gate voltage pulses of −1 V with Δt = 100 ms. (b) Spike frequency-dependent responses of channel conductance. (c, d) Potentiation and depression process of the synapse mimicked by successive gate voltage spikes with intervals of 1 s (V_g = 1 V, t_{on} = 400 ms).

tends to drop gradually with the increase of thickness of *t*-Se, which can be well explained by the higher intercalation efficiency of the Li^+ ion in thinner samples. These results indicate a clear transition from STP to LTP by employing a voltage pulse with large amplitude or width, which can be well explained by the Li^+ ion intercalation into a *t*-Se lattice.

The energy consumption is the key metric to evaluate the performance of a neuromorphic computing system. The "write" and "read" operations in three-terminal EGT devices are conducted separately. The energy consumption of neuromorphic networks is mainly determined by the "read" process due to the relatively small leakage current and large width of the voltage stimulation.[6,29] The power consumption per operation can be calculated by $P = V_{ds} \times \Delta I \times t_{on}$, where V_{ds}, ΔI, and t_{on} represent the source−drain voltage, EPSC, and the pulse width, respectively. With the data extracted from Figure 2b, we can plot the change ratio of energy consumption as a function of pulse width (Supporting Information Figure S8), and the smallest energy consumption was calculated to be only 0.1 pJ for a single pulse (2.0 V) event. This value is among the lowest of reported synaptic EGT devices with similar device configuration (Supporting Information Table S1).[30−34]

As applied with successive training cycles of gate voltage spikes, the channel conductance of the EGT device continues to decrease, and it reaches stability and cannot be restored back, which indicates a clear LTP characteristic of the devices. As shown in Figure 2e, the channel conductance cannot return back to the initial value after 10 consecutive voltage spikes, with the maximum value of ΔG reaching up to −27%. The applied positive voltage spikes were 1.5 V in height and 200 ms in width with an interval time of 1 s. This long-term ΔG of the EGT devices can be eliminated by the subsequent negative voltage, which results in the extraction of the Li ion and recovery of the channel conductance (Supporting Information Figure S9). These results indicate good reversibility of the conductance modulation by Li^+ ion intercalation/extraction. It is worthy to note that only the successive positive voltage spikes can lead to the long-term change of conductance in devices, while channel conductance can fully restore back to the original level after negative voltage stimulation within a short time (Supporting Information Figure S10), because the ClO_4^- ions have a relatively larger size and are very difficult to intercalate into a *t*-Se crystal lattice under negative voltage stimulation.

The paired pulse facilitation (PPF) phenomenon can be mimicked in *t*-Se EGT devices, which shows that the conductance change evoked by a pair of spikes can be increased when they are closely spaced.[35,36] The PPF index is defined as the ratio of the amplitude difference after paired spikes (A_2−A_1) and a conductance change of the first spike (A_1). As plotted in Figure 3a, the PPF index decreases gradually with the increase of interval time (Δt). For example, the PPF index is about 1.18 with a Δt of ∼10 ms, while it decreases to nearly 0 for a Δt above 800 ms. This feature endows the STP process of EGT devices with a high dependence on the stimulus frequency. Figure 3b shows the plot of the G of the device in response to 10 successive spikes (−1 V, 100 ms) with frequency ranging from 1 to 10 Hz, where the potentiation of ΔG can be clearly observed with the increase of frequency. In addition, repeatable modulation of the synaptic weight is another key merit for neuromorphic engineering applications.[37,38] Figure 3c and d present the

https://dx.doi.org/10.1021/acsnano.0c03124
ACS Nano 2020, 14, 10018−10026

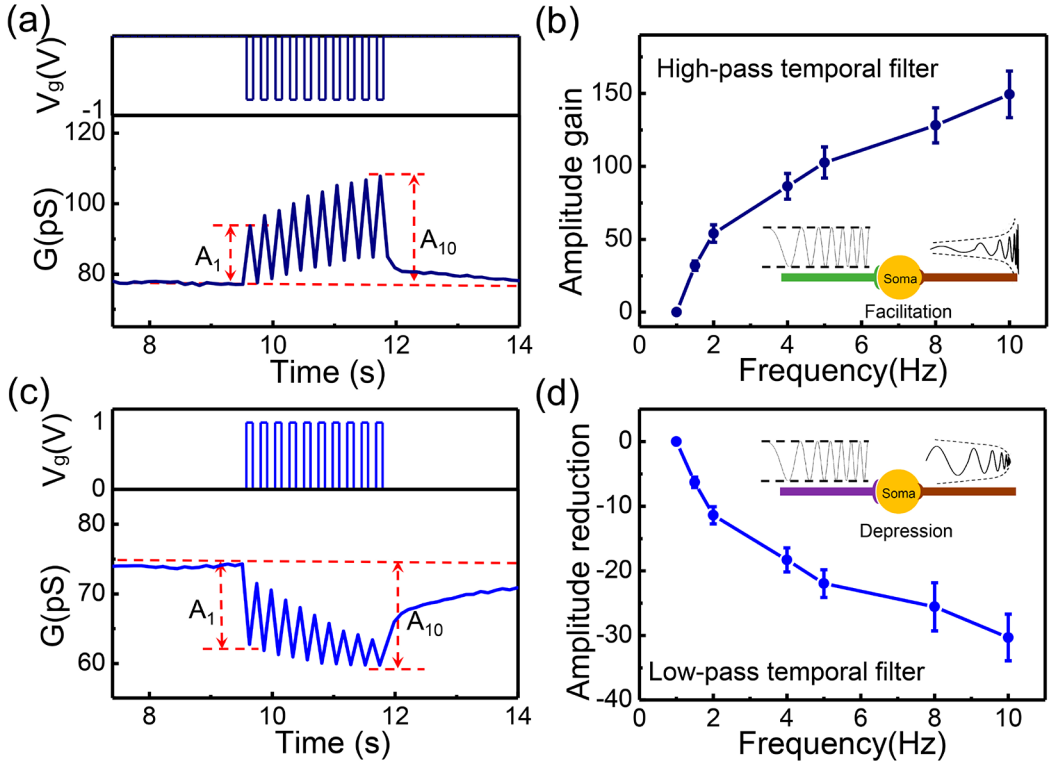

Figure 4. (a) Channel conductance recorded in response to 10 negative voltage trains with a frequency of 1 Hz. (b) Conductance amplitude gain (A_{10}/A_1) plotted as a function of presynaptic spike frequency. Inset image shows the schematic of high pass filtering of a synapse. (c) Channel conductance recorded in response to the stimulus train with positive voltage at a frequency of 1 Hz. (d) Conductance amplitude reduction (A_{10}/A_1) plotted as a function of presynaptic spike frequency. Inset image presents schematic diagram of low-pass filters in biological synapses.

response of G to consecutive gate voltage pulses. Every 20 positive gate spikes (1 V, 400 ms) followed by 20 negative gate spikes (−1 V, 400 ms) with a spacing of 1 s are applied. The bidirectional and symmetric switching of G between 60 and 120 pS can be successfully realized without degeneration for more than 10 cycles.

In a neurological system, synaptic efficacy can be modulated within milliseconds as applied with specific temporal patterns of a stimulus.[39−41] Synapses with strong short-term facilitation has a low probability of transmitter release, and it can act as a high-pass temporal filter for information processing. However, for the synapse with high probability of releasing, they usually have strong short-term depression and can be employed for a low-pass temporal filter. In this way, the transmission process of signals in neurons can be efficiently regulated, enabling a variety of possibilities to modify neural communication. This functional role of dynamic filtering in the synapse can be realized in our EGT devices. As applied with consecutive negative voltage spikes, the amplitude of conductance change in the *t*-Se EGT device increases gradually depending on the stimulation frequency (Figure 4a), indicating a high-pass temporal filter characteristic. The amplitude gain, defined as $(A_{10} - A_1)/A_1$, is utilized to describe the filtering property of device, where A_1 and A_{10} represent the conductance amplitude of the first and last spikes, respectively. As plotted in Figure 4b, the amplitude gain increases significantly at high frequency, reaching up to 150% at a frequency of 10 Hz. By setting the initial state as a low-resistance state and the voltage spike to a positive value, the low-pass filtering characteristics of input signals can be successfully emulated (Figure 4c and d). In sharp contrast to the high-pass filtration, the amplitude reduction decreases rapidly with the increase of frequency. For a frequency of 2, 5, and 10 Hz, the amplitude reduction is calculated to be −11%, −24%, and −32%, respectively. The high dependence of amplitude gain/reduction on frequency can be well explained by the strong coupling effect of mobile ions at high frequency in the electrolyte.[42] The successful emulation of temporal filtering in the synapse is of great significance for complex information processing, since it can efficiently screen input signals with different frequencies of excitation.

Different from other layered transition metal dichalcogenide (TMDC) materials with typical 2D vdW structure, the Se atoms in *t*-Se are covalently bonded along the *c*-axis into helical chains while stacked by a weak vdW interaction along the orthogonal plane (inset image in Figure 5c).[43,44] These vdW gaps between atomic chains can greatly facilitate the ion intercalation into crystal lattices under an applied gate voltage. In addition, the 1D vdW crystal structure with high asymmetry also renders a high anisotropy in its electrical conductance,[45−49] which enables the device to process spatiotemporal information. In order to study the relationship between atomic structure and electrical transport properties, the devices with a pair of diametrically opposite contact electrodes (numbered as 1, 2, 3, and 4) were fabricated based on a *t*-Se nanosheet with a thickness of approximately 30 nm (Supporting Information Figure S11a,b).

The transfer curves of the device with a Si back-gated configuration measured along two orthogonal directions at V_{ds} = 1 V indicate a distinct anisotropy in its electrical transport behavior (Supporting Information Figure S11c), and the corresponding output curve indicates an ideal ohmic contact at

https://dx.doi.org/10.1021/acsnano.0c03124
ACS Nano 2020, 14, 10018−10026

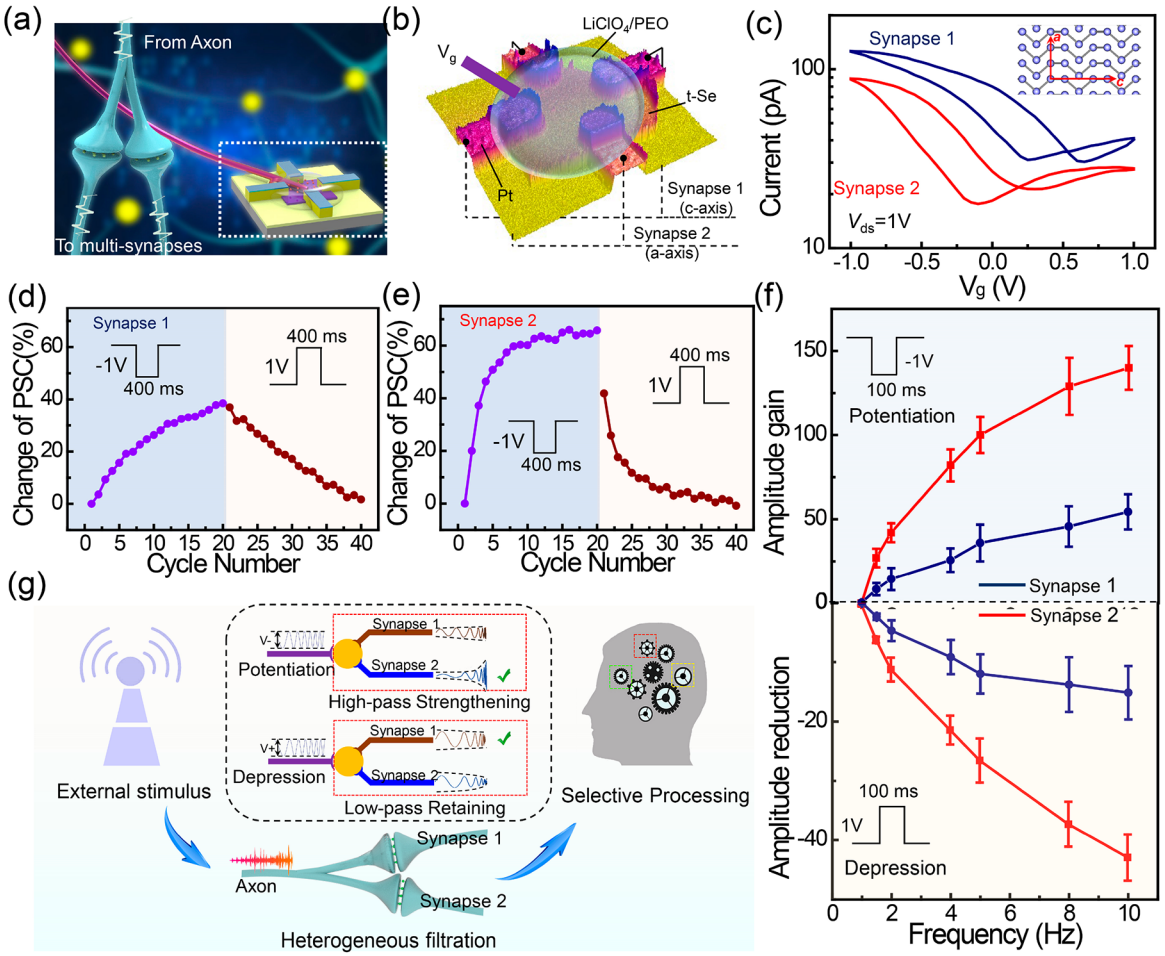

Figure 5. (a) Schematic illustrations of the axon−multisynapse system in the human brain, which can be mimicked by the multiple output *t*-Se EGT devices. (b) Schematics of EGT devices based on a *t*-Se nanosheet with a thickness of about 30 nm. Synapse 1 and synapse 2 are represented by devices along and across the *c*-axis of *t*-Se, respectively. (c) Typical transfer curves of the devices. (d, e) Conductance weight modulation of the devices subject to a train of negative (−1 V, 400 ms pulses with 1 s intervals) and positive (1 V, 400 ms pulses with 1 s intervals) pulses for synapse 1 and synapse 2, respectively. (f) Amplitude gain and reduction (A_{10}/A_1) of devices as a function of frequency (1, 2, 4, 5, 8, 10 Hz). (g) Biological axon−multisynapse system with selective memorizing ability toward the same inputs.

the Pt/*t*-Se interface (Supporting Information Figure S11d). The device exhibits a high ON/OFF ratio up to 10^4 with the gate voltage ranging from −100 to 20 V. The field-effect mobility (μ_{FE}) can be calculated from the linear region using eq 1:

$$\mu_{FE} = \frac{L}{W}\frac{1}{C_g V_{ds}}\frac{dI_{ds}}{dV_g} \quad (1)$$

where L, W, and C_g represent the channel length, channel width, and back-gate capacitance per unit area, respectively. The mobility μ_{13} = 0.64 $cm^2/(V\ s)$ can be demonstrated along the Se chain direction, while it decreases to μ_{24} = 0.11 $cm^2/(V\ s)$ when the direction is perpendicular to the Se chains. The conductance along the Se atomic chain is much larger than that of the orthogonal direction, and a maximum anisotropic ratio up to 8.6 can be obtained at a V_g of −100 V.

The dissimilarity of electrical conductance in *t*-Se enables the EGT devices to emulate the functions of the axon−multisynapse architecture in biological systems (Figure 5a).[19,50] Figure 5b shows the atomic force microscopy image of the EGT devices comprising a pair of opposite electrodes. The devices share the same channel area, which is covered by a $LiClO_4$/PEO electrolyte. The voltage pulse applied on the side gate acts as the stimulus spike from the common axon, and the anisotropic response of the channel conductance represents the transmission process of signals through various synapses. Here, synapses 1 and 2 are represented by the devices that are parallel and perpendicular to the *c*-axis direction of *t*-Se, respectively. Figure 5c plots the typical transfer characteristics of the *t*-Se EGT devices with V_g ranging from −1 to 1 V. The overall drain current along the *c*-axis direction is demonstrated to be much higher than that along the orthogonal direction. Due to the capping of BN layers on the electrodes, the influence of gate leakage current can be minimized to ensure the gate control over the channel conductance (Supporting Information Figure S12).

The modulation of synaptic weight in EGT devices under consecutive spikes also exhibits a high dependence on the crystalline direction. Figure 5d and e show the potentiation and depression process of EGT devices along and perpendicular to the *c*-axis of *t*-Se, respectively. As applied with a negative pulse, the weight for synapse 1 increases sublinearly, reaching up to 40% after the 20th stimulus. However, fast saturation of the conductance weight was observed in synapse 2 with a much higher maximum of 67%. The synaptic weight of both synapses gradually decreases and

https://dx.doi.org/10.1021/acsnano.0c03124
ACS Nano 2020, 14, 10018−10026

restores back to the initial value after 20 successive positive pulse. These results suggest that the change of conductance weight in *t*-Se EGT devices along the *a*-axis direction is much higher than that along the *c*-axis direction. As discussed before, the *t*-Se EGT devices can act as high-pass/low-pass temporal filters to transmit input signals with different frequencies. Figure 5f and Figure S13 in the Supporting Information compare the response of channel conductance in a multi-terminal device to a stimulus train with different frequencies (1, 2, 4, 5, 8, and 10 Hz). As a high-pass filter, the amplitude gains of synapse 2 increases sharply at high frequency, with the highest value of 280% at 10 Hz. However, the synapse 1 exhibits a very weak response to the frequency, and the amplitude gain can only increase from 0 to 150% with the frequency from 1 to 10 Hz. During the depression process with a positive voltage pulse, both synapses can work as low-pass filters, and the amplitude reduction of synapse 2 increases much faster than that of synapse 1. More devices with the thickness of the *t*-Se nanosheet ranging from 22 to 40 nm exhibit distinct anisotropy in their filtering ability, suggesting a good reproducibility of the synaptic weight modulation (Supporting Information Figures S14 and S15).

This highly anisotropic modulation of synaptic weight enables the *t*-Se devices to process information with high heterogeneity. As illustrated in Figure 5g, the perception stimulus from the external environment can be first received and converted into the presynaptic potentials in the axon, which are further passed to the postsynapses through the modulation of synaptic weight. This process can be well mimicked using the multiple-output EGT device based on a *t*-Se nanosheet. The voltage stimulus, which resembles the potentials from the axon, is well sorted and applied onto the electrolyte gate of *t*-Se devices along different crystalline directions, and the signals can be further decoded with strong heterogeneity due to the intrinsic dissimilarity of *t*-Se, resulting in the selectivity of information processing. This compact multiple-output EGT device is of great significance to realize the selective processing in bioinspired neural systems.

CONCLUSIONS

In summary, a group-IV elemental *t*-Se nanosheet was introduced to fabricate an EGT with extremely low energy consumption. It demonstrates that the conductance can be efficiently modulated by the formation of EDL and the Li^+ ion intercalation into *t*-Se. Due to the intrinsic heterogeneity of electrical conductance, the EGT device based on a *t*-Se nanosheet exhibits a high anisotropy in the modulation of synaptic weight as well as temporal filtering ability. The function of the biological axon−multisynapse network was also successfully emulated. This finding provides an attractive approach to realize the complex artificial neural system for mimicking the behaviors of the human brain.

EXPERIMENTAL METHODS

PVD Growth of *t*-Se Nanosheets. High-quality *t*-Se nanosheets were prepared using a modified PVD approach. The 99.99% Se power purchased from Sigma-Aldrich was placed at the center of a small quartz tube with double-side openings, and fresh Si(111) substrate etched by a buffered oxide etching (BOE) solution was placed at the end of the quartz tube. Then, the quartz tube was inserted into the heating center of a larger tube. The growth process was carried out with a temperature of 210 °C for 60 min until a pressure of less than 10 mbar.

Device Fabrication. The as-grown *t*-Se nanosheets were transferred onto the Si substrates covered by 300 nm SiO_2 by direct dry transfer, and the thicknesses of nanosheets can be determined using optical microscopy and atomic force microscopy (AFM) measurements. The Pt electrodes were patterned by standard electron beam lithography (EBL) with a thickness of about 50 nm. The device is patterned with a channel length of 10 μm, and the distance between side gate and channel is 20 μm. To prepare the polymer electrolyte, PEO (M_w = 100 000, Sigma-Aldrich) was first mixed with $LiClO_4$ with a mass ratio of 9:1. The mixture was then dissolved in 15 mL of anhydrous methanol and stirred for 24 h at 70 °C. Layers of BN were directly transferred using a dry transfer technique on the top of a source−drain electrode to minimize the influence of leakage current, and then the electrolyte liquid was dip-coated on the device surface. The devices were subsequently heated at 100 °C for 10 min to fully evaporate the methanol.

Electrical Measurements. Before electrical measurement, the *t*-Se devices were vacuumed for 12 h to remove the absorbed water molecules. All the electrical measurements were performed using a Keithley 4200 semiconductor parameter analyzer with a source measurement unit in a Lakeshore probe station. For the transfer curves, the sweeping rate was 20 mV s^{-1}.

DFT Calculation. The first-principle calculations were performed by using the Vienna *ab initio* simulation package (VASP). For the exchange−correlation energy, we employ the Perdew−Burke−Ernzerhof parametrization of the generalized gradient approximation. For structure relaxation, the force and the energy tolerance on each atom are less than 0.01 eV/Å and 10^{-5} eV, respectively. The energy cutoff of the plane wave basis is chosen to be 550 eV. A gamma-centered 6 × 6 × 6 Monkhorst−Pack *k*-point mesh was applied for the *k*-point samples in the Brillouin zone.

ASSOCIATED CONTENT

Supporting Information

The Supporting Information is available free of charge at https://pubs.acs.org/doi/10.1021/acsnano.0c03124.

Additional information (PDF)

AUTHOR INFORMATION

Corresponding Author

Yang Chai − *Department of Applied Physics, The Hong Kong Polytechnic University, Kowloon, Hong Kong 999077, People's Republic of China; The Hong Kong Polytechnic University Shenzhen Research Institute, Shenzhen 518055, People's Republic of China;* orcid.org/0000-0002-8943-0861; Email: ychai@polyu.edu.hk

Authors

Jing-Kai Qin − *Department of Applied Physics, The Hong Kong Polytechnic University, Kowloon, Hong Kong 999077, People's Republic of China; School of Materials Science and Engineering, Harbin Institute of Technology (Shen Zhen), Shen Zhen 518055, People's Republic of China*

Feichi Zhou − *Department of Applied Physics, The Hong Kong Polytechnic University, Kowloon, Hong Kong 999077, People's Republic of China*

Jingli Wang − *Department of Applied Physics, The Hong Kong Polytechnic University, Kowloon, Hong Kong 999077, People's Republic of China; The Hong Kong Polytechnic University Shenzhen Research Institute, Shenzhen 518055, People's Republic of China*

Jiewei Chen − *Department of Applied Physics, The Hong Kong Polytechnic University, Kowloon, Hong Kong 999077, People's Republic of China*

https://dx.doi.org/10.1021/acsnano.0c03124
ACS Nano 2020, 14, 10018−10026

Cong Wang − *Department of Applied Physics, The Hong Kong Polytechnic University, Kowloon, Hong Kong 999077, People's Republic of China*
Xuyun Guo − *Department of Applied Physics, The Hong Kong Polytechnic University, Kowloon, Hong Kong 999077, People's Republic of China;* orcid.org/0000-0003-0365-7545
Shouxin Zhao − *School of Materials Science and Engineering, Harbin Institute of Technology (Shen Zhen), Shen Zhen 518055, People's Republic of China*
Yi Pei − *School of Materials Science and Engineering, Harbin Institute of Technology (Shen Zhen), Shen Zhen 518055, People's Republic of China*
Liang Zhen − *School of Materials Science and Engineering, Harbin Institute of Technology (Shen Zhen), Shen Zhen 518055, People's Republic of China;* orcid.org/0000-0001-6159-8972
Peide D. Ye − *School of Electrical and Computer Engineering, Purdue University, West Lafayette, Indiana 47907, United States;* orcid.org/0000-0001-8466-9745
Shu Ping Lau − *Department of Applied Physics, The Hong Kong Polytechnic University, Kowloon, Hong Kong 999077, People's Republic of China; The Hong Kong Polytechnic University Shenzhen Research Institute, Shenzhen 518055, People's Republic of China*
Ye Zhu − *Department of Applied Physics, The Hong Kong Polytechnic University, Kowloon, Hong Kong 999077, People's Republic of China*
Cheng-Yan Xu − *School of Materials Science and Engineering, Harbin Institute of Technology (Shen Zhen), Shen Zhen 518055, People's Republic of China;* orcid.org/0000-0002-7835-6635

Complete contact information is available at: https://pubs.acs.org/10.1021/acsnano.0c03124

Author Contributions

Y.C. and J.K.Q. conceived the idea. S.X.Z., Y.P., C.Y.X., L.Z., and P.D.Y. performed and supervised the growth experiments. J.K.Q., J.L.W., F.C.Z., and J.W.C. performed device fabrication and analyzed the experimental data. C.W. performed the theoretical calculation. X.G. and Y.Z. conducted and supervised the TEM characterization. J.K.Q. and Y.C. wrote the manuscript.

Notes

The authors declare no competing financial interest.

ACKNOWLEDGMENTS

The work was supported by Research Grant Council of Hong Kong (PolyU 152053/18E), Science, Technology and Innovation Commission of Shenzhen (JCYJ20180507183424383), National Natural Science Foundation of China (61851402), and the Hong Kong Polytechnic University (1-ZVGH and G-SB79).

REFERENCES

(1) Zhou, F.; Zhou, Z.; Chen, J.; Choy, T. H.; Wang, J.; Zhang, N.; Lin, Z.; Yu, S.; Kang, J.; Wong, H.-S. P.; Chai, Y. Optoelectronic Resistive Random Access Memory for Neuromorphic Vision Sensors. *Nat. Nanotechnol.* **2019**, *14*, 776−782.
(2) Wang, Z.; Joshi, S.; Savel'ev, S. E.; Jiang, H.; Midya, R.; Lin, P.; Hu, M.; Ge, N.; Strachan, J. P.; Li, Z.; Wu, Q.; Barnell, M.; Li, G.-L.; Xin, H. L.; Williams, R. S.; Xia, Q.; Yang, J. J. Memristors with Diffusive Dynamics as Synaptic Emulators for Neuromorphic Computing. *Nat. Mater.* **2017**, *16*, 101−108.
(3) van de Burgt, Y.; Melianas, A.; Keene, S. T.; Malliaras, G.; Salleo, A. Organic Electronics for Neuromorphic Computing. *Nat. Electron.* **2018**, *1*, 386−397.
(4) Kim, S.; Du, C.; Sheridan, P.; Ma, W.; Choi, S.; Lu, W. D. Experimental Demonstration of a Second-Order Memristor and Its Ability to Biorealistically Implement Synaptic Plasticity. *Nano Lett.* **2015**, *15*, 2203−2211.
(5) Merolla, P. A.; Arthur, J. V.; Alvarez-Icaza, R.; Cassidy, A. S.; Sawada, J.; Akopyan, F.; Jackson, B. L.; Imam, N.; Guo, C.; Nakamura, Y.; Brezzo, B.; Vo, I.; Esser, S. K.; Appuswamy, R.; Taba, B.; Amir, A.; Flickner, M. D.; Risk, W. P.; Manohar, R.; Modha, D. S. A Million Spiking-Neuron Integrated Circuit with a Scalable Communication Network and Interface. *Science* **2014**, *345*, 668−673.
(6) Yang, C.-S.; Shang, D.-S.; Liu, N.; Fuller, E. J.; Agrawal, S.; Talin, A. A.; Li, Y. Q.; Shen, B.-G.; Sun, Y. All-Solid-State Synaptic Transistor with Ultralow Conductance for Neuromorphic Computing. *Adv. Funct. Mater.* **2018**, *28*, 1804170.
(7) Yang, J.-T.; Ge, C.; Du, J.-Y.; Huang, H. Y.; He, M.; Wang, C.; Lu, H.-B.; Yang, G.-Z.; Jin, K.-J. Artificial Synapses Emulated by an Electrolyte-Gated Tungsten-Oxide Transistor. *Adv. Mater.* **2018**, *30*, 1801548.
(8) Zhu, J.; Yang, Y.; Jia, R.; Liang, Z.; Zhu, W.; Rehman, Z. U.; Bao, L.; Zhang, X.; Cai, Y.; Song, L.; Huang, R. Ion Gated Synaptic Transistors Based on 2D van der Waals Crystals with Tunable Diffusive Dynamics. *Adv. Mater.* **2018**, *30*, 1800195.
(9) Sharbati, M. T.; Du, Y.; Torres, J.; Ardolino, N. D.; Yun, M.; Xiong, F. Artificial Synapses: Low-Power, Electrochemically Tunable Graphene Synapses for Neuromorphic Computing. *Adv. Mater.* **2018**, *30*, 1870273.
(10) Yu, F.; Zhu, L. Q.; Xiao, H.; Gao, W. T.; Guo, Y. B. Restickable Oxide Neuromorphic Transistors with Spike-Timing-Dependent Plasticity and Pavlovian Associative Learning Activities. *Adv. Funct. Mater.* **2018**, *28*, 1804025.
(11) Fu, Y. M.; Wan, C. J.; Zhu, L. Q.; Xiao, H.; Chen, X. D.; Wan, Q. Hodgkin-Huxley Artificial Synaptic Membrane Based on Protonic/Electronic Hybrid Neuromorphic Transistors. *Adv. Biosys.* **2018**, *2*, 1700198.
(12) Jiang, J.; Bai, Z. L.; Chen, Z. H.; He, L.; Zhang, D. W.; Zhang, Q. H.; Shi, J. A.; Park, M. H.; Scott, J. F.; Hwang, C. S.; Jiang, A. Q. Temporary Formation of Highly Conducting Domain Walls for Non-Destructive Read-Out of Ferroelectric Domain-Wall Resistance Switching Memories. *Nat. Mater.* **2018**, *17*, 49−56.
(13) Shi, Y.; Liang, X.; Yuan, B.; Chen, V.; Li, H.; Hui, F.; Yu, Z.; Yuan, F.; Pop, E.; Wong, H.-S. P.; Lanza, M. Electronic Synapses Made of Layered Two-Dimensional Materials. *Nat. Electron.* **2018**, *1*, 458−465.
(14) Jo, S. H.; Chang, T.; Ebong, I.; Bhadviya, B. B.; Mazumder, P.; Lu, W. Nanoscale Memristor Device as Synapse in Neuromorphic Systems. *Nano Lett.* **2010**, *10*, 1297−1301.
(15) van de Burgt, Y.; Lubberman, E.; Fuller, E. J.; Keene, S. T.; Faria, G. C.; Agarwal, S.; Marinella, M. J.; Talin, A. A.; Salleo, A. A Non-Volatile Organic Electrochemical Device as a Low-Voltage Artificial Synapse for Neuromorphic Computing. *Nat. Mater.* **2017**, *16*, 414−418.
(16) Guerrero, G.; Reiff, D. F.; Agarwal, G.; Ball, R. W.; Borst, A.; Goodman, C. S.; Isacoff, E. Y. Heterogeneity in Synaptic Transmission along a Drosophila Larval Motor Axon. *Nat. Neurosci.* **2005**, *8*, 1188−1196.
(17) Murthy, V. N.; Sejnowski, T. J.; Stevens, C. F. Heterogeneous Release Properties of Visualized Individual Hippocampal Synapses. *Neuron* **1997**, *18*, 599−612.
(18) Pfeil, T.; Jordan, J.; Tetzlaff, T.; Grübl, A.; Schemmel, J.; Diesmann, M.; Meier, K. Effect of Heterogeneity on Decorrelation Mechanisms in Spiking Neural Networks: A Neuromorphic-Hardware Study. *Phys. Rev. X* **2016**, *6*, 021023.
(19) Tian, H.; Guo, Q.; Xie, Y.; Zhao, H.; Li, C.; Cha, J. J.; Xia, F.; Wang, H. Anisotropic Black Phosphorus Synaptic Device for Neuromorphic Applications. *Adv. Mater.* **2016**, *28*, 4991−4997.

(20) Changeux, J.-P.; Danchin, A. Selective Stabilisation of Developing Synapses as a Mechanism for the specification of Neuronal networks. *Nature* **1976**, *264*, 705−712.
(21) Qin, J.; Qiu, G.; Jian, J.; Zhou, H.; Yang, L.; Charnas, A.; Zemlyanov, D. Y.; Xu, C.-Y.; Xu, X.; Wu, W.; Wang, H. Y.; Ye, P. D. Controlled Growth of a Large-Size 2D Selenium Nanosheet and Its Electronic and Optoelectronic Applications. *ACS Nano* **2017**, *11*, 10222−10229.
(22) Chang, T.; Jo, S.-H.; Lu, W. Short-Term Memory to Long-Term Memory Transition in a Nanoscale Memristor. *ACS Nano* **2011**, *5*, 7669−7676.
(23) Liu, Y. H.; Zhu, L. Q.; Feng, P.; Shi, Y.; Wan, Q. Freestanding Artificial Synapses Based on Laterally Proton-Coupled Transistors on Chitosan Membranes. *Adv. Mater.* **2015**, *27*, 5599−5604.
(24) Li, Q.; Liu, H.; Yao, Z.; Cheng, J.; Li, T.; Li, Y.; Wolverton, C.; Wu, J.; Dravid, V. P. Electrochemistry of Selenium with Sodium and Lithium: Kinetics and Reaction Mechanism. *ACS Nano* **2016**, *10*, 8788−8795.
(25) Abouimrane, A.; Dambournet, D.; Chapman, K. W.; Chupas, P. J.; Weng, W.; Amine, K. A New Class of Lithium and Sodium Rechargeable Batteries Based on Selenium and Selenium-Sulfur as a Positive Electrode. *J. Am. Chem. Soc.* **2012**, *134*, 4505−4508.
(26) Li, Y.; Lu, J.; Cheng, X.; Shi, H.; Zhang, Y. Interfacial Lithiation Induced Leapfrog Phase Transformation in Carbon Coated Se Cathode Observed by *In-Situ* TEM. *Nano Energy* **2018**, *48*, 441−447.
(27) Li, X.; Liang, J.; Li, X.; Wang, C.; Luo, J.; Li, R.; Sun, X. High-Performance All-Solid-State Li-Se Batteries Induced by Sulfide Electrolytes. *Energy Environ. Sci.* **2018**, *11*, 2828−2832.
(28) Yang, C.-P.; Xin, S.; Yin, Y.-X.; Ye, H.; Zhang, J.; Guo, Y.-G. An Advanced Selenium-Carbon Cathode for Rechargeable Lithium-Selenium Batteries. *Angew. Chem., Int. Ed.* **2013**, *52*, 8363−8367.
(29) Nikam, R. D.; Kwak, M.; Lee, J.; Rajput, K. G.; Hwang, H. Controlled Ionic Tunneling in Lithium Nanoionic Synaptic Transistor Through Atomically Thin Graphene Layer for Neuromorphic Computing. *Adv. Electron. Mater.* **2020**, *6*, 1901100.
(30) Yang, C. S.; Shang, D. S.; Liu, N.; Shi, G.; Shen, X.; Yu, R. C.; Li, Y. Q.; Sun, Y. A Synaptic Transistor Based on Quasi-2D Molybdenum Oxide. *Adv. Mater.* **2017**, *29*, 1700906.
(31) Gkoupidenis, P.; Schaefer, N.; Garlan, B.; Malliaras, G. G. Neuromorphic Functions in PEDOT: PSS Organic Electrochemical Transistors. *Adv. Mater.* **2015**, *27*, 7176−7180.
(32) Balakrishna Pillai, P.; De Souza, M. M. Nanoionics-Based Three-Terminal Synaptic Device Using Zinc Oxide. *ACS Appl. Mater. Interfaces* **2017**, *9*, 1609−1618.
(33) Lai, Q.; Zhang, L.; Li, Z.; Stickle, W. F.; Williams, R. S.; Chen, Y. Ionic/Electronic Hybrid Materials Integrated in a Synaptic Transistor with Signal Processing and Learning Functions. *Adv. Mater.* **2010**, *22*, 2448−2453.
(34) Zhu, L. Q.; Wan, C. J.; Guo, L. Q.; Shi, Y.; Wan, Q. Artificial Synapse Network on Inorganic Proton Conductor for Neuromorphic Systems. *Nat. Commun.* **2014**, *5*, 1−7.
(35) Oertner, T. G.; Sabatini, B. L.; Nimchinsky, E. A.; Svoboda, K. Facilitation at Single Synapses Probed with Optical Quantal Analysis. *Nat. Neurosci.* **2002**, *5*, 657−664.
(36) Rosahl, T. W.; Geppert, M.; Spillane, D.; Herz, J.; Hammer, R. E.; Malenka, R. C.; Südhof, T. C. Short-Term Synaptic Plasticity is Altered in Mice Lacking Synapsin I. *Cell* **1993**, *75*, 661−670.
(37) Tan, H.; Ni, Z.; Peng, W.; Du, S.; Liu, X.; Zhao, S.; Li, W.; Ye, Z.; Xu, M.; Xu, Y.; Pi, X.; Yang, D. Broadband Optoelectronic Synaptic Devices Based on Silicon Nanocrystals for Neuromorphic Computing. *Nano Energy* **2018**, *52*, 422−430.
(38) Lee, M.; Lee, W.; Choi, S.; Jo, J.-W.; Kim, J.; Park, S. K.; Kim, Y. H. Brain-Inspired Photonic Neuromorphic Devices Using Photodynamic Amorphous Oxide Semiconductors and Their Persistent Photoconductivity. *Adv. Mater.* **2017**, *29*, 1700951.
(39) Abbott, L. F.; Regehr, W. G. Synaptic Computation. *Nature* **2004**, *431*, 796−803.
(40) Fortune, E. S.; Rose, G. J. Short-Term Synaptic Plasticity Contributes to the Temporal Filtering of Electrosensory Information. *J. Neurosci.* **2000**, *20*, 7122−7130.
(41) Jiang, J.; Guo, J.; Wan, X.; Yang, Y.; Xie, H.; Niu, D.; Yang, J.; He, J.; Gao, Y.; Wan, Q. 2D MoS_2 Neuromorphic Devices for Brain-Like Computational Systems. *Small* **2017**, *13*, 1700933.
(42) Feng, P.; Xu, W.; Yang, Y.; Wan, X.; Shi, Y.; Wan, Q.; Zhao, J.; Cui, Z. Printed Neuromorphic Devices Based on Printed Carbon Nanotube Thin-Film Transistors. *Adv. Funct. Mater.* **2017**, *27*, 1604447.
(43) Bhaskar, P.; Achtstein, A. W.; Diedenhofen, S. L.; Siebbeles, L. D. A. Mobility and Decay Dynamics of Charge Carriers in One-Dimensional Selenium van der Waals Solid. *J. Phys. Chem. C* **2017**, *121*, 18917−18921.
(44) Qin, J.-K.; Qiu, G.; He, W.; Jian, J.; Si, M. W.; Duan, Y. Q.; Charnas, A.; Zemlyanov, D. Y.; Wang, H. Y.; Shao, W.-Z.; Zhen, L.; Xu, C.-Y.; Ye, P. D. Epitaxial Growth of 1D Atomic Chain Based Se Nanoplates on Monolayer ReS_2 for High-Performance Photodetectors. *Adv. Funct. Mater.* **2018**, *28*, 1806254.
(45) Murphy, K. E.; Wunderlich, B. B.; Wunderlich, B. Effect of Structure on the Electrical Conductivity of Selenium. *J. Phys. Chem.* **1982**, *86*, 2827−2835.
(46) Plessner, K. W. Conductivity, Hall Effect and Thermo-Electric Power of Selenium Single Crystals. *Proc. Phys. Soc., London, Sect. B* **1951**, *64*, 671.
(47) Henkels, H. W.; Maczuk, J. Anisotropic Resistivities of Selenium Crystals at High Frequencies. *Phys. Rev.* **1953**, *91*, 1562.
(48) Bammes, P.; Klucker, R.; Koch, E.; Tuomi, T. Anisotropy of the Dielectric Constants of Trigonal Selenium and Tellurium Between 3 and 30 eV. *Phys. Status Solidi B* **1972**, *49*, 561−570.
(49) Wang, J.; Qiao, J.; Xu, K.; Chen, J.; Zhao, Y.; Qiu, B.; Lin, Z.; Ji, W.; Chai, Y. Quasi One-Dimensional van der Waals Gold Selenide with Strong Interchain Interaction and Giant Magnetoresistance. *Sci. Bull.* **2020**, *65*, 1451−1459.
(50) Markram, H.; Wang, Y.; Tsodyks, M. Differential Signaling *via* the Same Axon of Neocortical Pyramidal Neurons. *Proc. Natl. Acad. Sci. U. S. A.* **1998**, *9*, 5323.

https://dx.doi.org/10.1021/acsnano.0c03124
ACS Nano 2020, 14, 10018−10026